PNAS Nexus, 2023, 2, 1–12
https://doi.org/10.1093/pnasnexus/pgad317
Advance access publication 9 October 2023
Research Report

A biomimetic chip to assess subcutaneous bioavailability of monoclonal antibodies in humans

Vineeth Chandran Suja[a,b,†], Qin M Qi[a,b,†,1], Kevin Halloran[c,2], Jifeng Zhang[c,3], Suyog Shaha[a,b], Supriya Prakash[a,b], Ninad Kumbhojkar[a,b], Antoine Deslandes[d], Sylvain Huille[d], Yatin R. Gokarn[c,4] and Samir Mitragotri[a,b,*]

[a]School of Engineering and Applied Sciences, Harvard University, Boston, MA 02134, USA
[b]Wyss Institute for Biologically Inspired Engineering, 3 Blackfan Circle, Boston, MA 02115, USA
[c]Sanofi, 350 Water St, Cambridge, MA 02141, USA
[d]Sanofi R&D, Impasse Des Ateliers, Vitry-sur-Seine 94400 France
*To whom correspondence should be addressed: Email: mitragotri@seas.harvard.edu
†V.C.S. and Q.M.Q. contributed equally to this work.
[1]Present address: Department of Chemical Engineering, MIT, MA 02142, USA.
[2]Present address: AbbVie, 200 Sidney St, Cambridge, MA 02139, USA.
[3]Present address: Shanghai Henlius Biopharmaceutical Co., Ltd, 1289 Yishan Road, Xuhui District, Shanghai 200233, China.
[4]Present address: Alexion Pharmaceuticals Inc, 121 Seaport Blvd, Boston, MA 02210, USA.
Edited By: Rui Reis

Abstract

Subcutaneous (subQ) injection is a common route for delivering biotherapeutics, wherein pharmacokinetics is largely influenced by drug transport in a complex subQ tissue microenvironment. The selection of good drug candidates with beneficial pharmacokinetics for subQ injections is currently limited by a lack of reliable testing models. To address this limitation, we report here a *Sub*cutaneous Co-*Cul*ture Tissue-on-a-chip for *I*njection Simulation (SubCuTIS). SubCuTIS possesses a 3D coculture tissue architecture, and it allows facile quantitative determination of relevant scale independent drug transport rate constants. SubCuTIS captures key in vivo physiological characteristics of the subQ tissues, and it differentiates the transport behavior of various chemically distinct molecules. We supplemented the transport measurements with theoretical modeling, which identified subtle differences in the local absorption rate constants of seven clinically available mAbs. Accounting for first-order proteolytic catabolism, we established a mathematical framework to assess clinical bioavailability using the local absorption rate constants obtained from SubCuTIS. Taken together, the technology described here broadens the applicability of organs-on-chips as a standardized and easy-to-use device for quantitative analysis of subQ drug transport.

Significance Statement

Subcutaneous (subQ) injection is an emerging attractive alternative to intravenous (IV) injections for delivering monoclonal antibodies (mAbs). SubQ injections can be self-administered, which mitigates hospital visits that are necessary for IV injections. However, development of subQ mAb formulations is hampered by the limitations of existing animal models primarily, injection site-to-site variability, poor correlation with human pharmacokinetics (PK), cost, and ethical concerns. We report here a microfluidic platform that addresses these limitations and provides a suitable framework to assess transport properties and human bioavailability of mAb formulations administered in the subQ space. Our study opens new possibilities for the use of microfluidic devices to recapitulate complex tissues in a reliable manner, consistent with the goals of the FDA modernization act.

Introduction

Subcutaneous (subQ) injection is a common mode of administering biologics such as insulin and interferons, and it is an emerging route for administering antibodies (1–4). Drugs diffuse through the subQ tissue, located beneath the skin dermis (5), prior to drainage into the vascular or lymphatic capillaries and ultimately into systemic circulation (1–3). As a result, the subQ tissue microstructure plays a vital role in drug pharmacokinetics (1, 4). Adipocytes form the major component of the subQ tissue, followed by fibroblasts (4, 6). Injected macromolecules undergo hindered diffusion through the interstitial space in the extracellular matrix (ECM) formed by these cells and finally enter systemic circulation by crossing the endothelial wall lining of blood and lymphatic vessels (4, 7). Due to these multiple barriers to drug transport, some biologics, especially antibodies, do not exhibit satisfactory bioavailability after subQ injection (7). Incorporation

Competing Interest: Q.M.Q. and S.M. are inventors on a patent application related to the technology described in this manuscript (owned and managed by Harvard University). All other authors have no competing interests to disclose.
Received: May 23, 2023. **Accepted:** September 12, 2023

of strategies to improve pharmacokinetics during the drug development process is limited by the lack of reliable preclinical testing models (7). Animal studies (8–11) show poor correlation with human data (Fig. S1) due to anatomical and physiological differences between species (1, 4). A limited number of in vitro models, such as subcutaneous injection site simulator (SCISSOR), have been reported to mimic subQ transport and pharmacokinetics (12–14). These existing models typically use a buffer solution enclosed in a synthetic membrane to simulate diffusion within the ECM. Drug transport in these models depends on the properties of their synthetic components (14), and it lacks a mechanistic basis since the in vivo transport is determined both by subQ cells and the ECM, which consists of glycosaminoglycans, collagen and elastin (1). Furthermore, such models fail to capture and differentiate multiple steps and pathways of drug transport in the complex biological tissue. Computational models are an attractive alternative for predicting subQ pharmacokinetics (15–18). However, faithfully simulating the multifaceted mAb interactions with the complex subQ tissue is challenging (19), and there are currently no frameworks available for predicting subQ bioavailability. Part of the complexity arises from the fact that even nearly identical mAbs exhibit differences in their sequences, 3D structures, and spatial aggregation propensity. When coupled with the immense heterogeneity and complexity of the subQ extracellular matrix (ECM), predicting the diverse interactions that govern the transport, absorption, and elimination of mAbs becomes an incredibly difficult task.

With the recent passage of the FDA 2.0 modernization act (20), there is a renewed and pressing interest in developing robust and high fidelity in vitro human microphysiological systems for drug development. Microphysiological systems, such as organs-on-chips, can mimic organ functions under physiological conditions and thus hold great promise for predicting drug transport and pharmacokinetics in vitro (21–26). Among various established organ models, fat-on-a-chip is most relevant to the subQ tissue, given its primary cellular components are adipocytes (27–31). Due to issues such as buoyancy, fragility and limited long-term functionality, microfluidic culturing of adipocytes is a nontrivial task (28, 30, 31). Further, fat-on-a-chip lacks the structural complexity necessary to mimic all aspects of subQ drug transport. Chips comprising multicomponent 3D architecture are needed to capture the complexity of drug transport in the subQ tissue. In addition, new data analysis methods are needed to accurately determine various transport coefficients and quantitatively estimate drug pharmacokinetics.

To fulfill the pressing need for an effective in vitro framework, we present a *Sub*cutaneous Co-*Cu*lture *T*issue-on-a-chip for *I*njection Simulation (SubCuTIS), the first in vitro coculture subQ tissue model, to our knowledge, to evaluate subQ drug transport and pharmacokinetics. This modular model can simulate both human and animal subQ environment, and it allows us to account for multiple interactions between mAbs and the subQ ECM. The model comprises a three-compartment microfluidic chip that captures all essential components of subQ drug transport: (i) an injection compartment containing the drug solution representing the drug depot postinjection; (ii) a subQ compartment containing adipocytes and fibroblasts cocultured in a 3D hydrogel matrix representing the fat, the connective tissues and the interstitial space; and (iii) a vessel/vascular compartment representing either the lymphatics (in the absence of a cell lining) or the vasculature (in the presence of an endothelial cell lining). We overcame the challenge of maintaining delicate adipocytes in a cocultured environment using a novel method of hydrogel-supported cell encapsulation (32) followed by induction of adipocyte differentiation in situ (27, 29, 31, 32). We further extended the viability of microfluidic cell culture to more than 10 days by implementing a protocol based solely on perfusion at various flow rates. We quantitatively determined multiple scale independent transport coefficients through an automated end-to-end time-correlated image processing protocol, bypassing the need for time-consuming numerical simulations. Finally, we established a mathematical framework to relate the measured transport coefficients to important PK parameters. In addition to reducing research timeline and costs compared to existing in vitro and animal models (3, 13), SubCuTIS demonstrates increased reproducibility and specificity as established by its ability to differentiate the effects of drug molecular weight (MW), charge, and shape on transport. More importantly, our findings provide new insights into drug pharmacokinetics that can hardly be investigated otherwise. Specifically, we compared the roles of vascular and lymphatic pathways of entry into systemic circulation (1–4), predicted the overall rate of absorption (8) and related the measurements to clinically measured bioavailability. Overall, our technology not only benefits the process of drug development for subQ administration but also opens up new possibilities for wide adoption of standard microfluidic devices to recapitulate complex organ functions in a versatile, reliable, and reproducible manner, consistent with the goals of the FDA modernization act.

Results

Mimicking subQ injection in an idealized geometry on a chip

SubQ injections deliver a small bolus of drug (typically 0.5 to 1 ml) to the fat tissue below the skin (Fig. 1a). The injected drug diffuses through the tissue before entering systemic circulation by partitioning across the blood and lymphatic vasculature. To capture the above key features, we employed a 3-chamber microfluidic configuration separated by 3 μm slits for permitting macromolecular transport while restricting cell migration across the chambers (Fig. 1b). The first compartment comprises a 200 μm injection chamber that contains the therapeutic formulation, the second compartment comprises a 500 μm subQ chamber that contains a 3D coculture of adipocytes and fibroblasts which collectively mimic the fat tissue, and the final compartment comprises a 200 μm vascular chamber that mimics either the lymphatics (in the absence of a cell lining) or the vasculature (in the presence of an endothelial cell lining).

Directly injecting drugs into the subQ chamber to form a depot is not feasible in microfluidic chips due to size constraints (~ 100 μm channel height) and due to undesirable tissue fracturing that can occur during injection. The latter can severely compromise the repeatable calculation of the transport rate constants. The distinct injection chamber in SubCuTIS helps us to conveniently circumvent these problems while maintaining a physiological drug depot. The subQ channel in SubCuTIS has a fixed size of 0.5 mm. The average thickness of human subQ tissue on the other hand can range anywhere from 1 mm to over 20 mm (33). While this disparity might initially seem significant, its essential to note that the core objective of SubCuTIS is to enable the measurement of the scale independent transport rate constants associated with subQ transport of mAbs. This approach, similar to the acellular SCISSOR platform (12), overcomes challenges tied to creating and imaging subQ tissue at physiological scale. It is also worth noting that the absence of lymphatic cells in SubCuTIS is aphysical but not limiting. The slit dimensions in

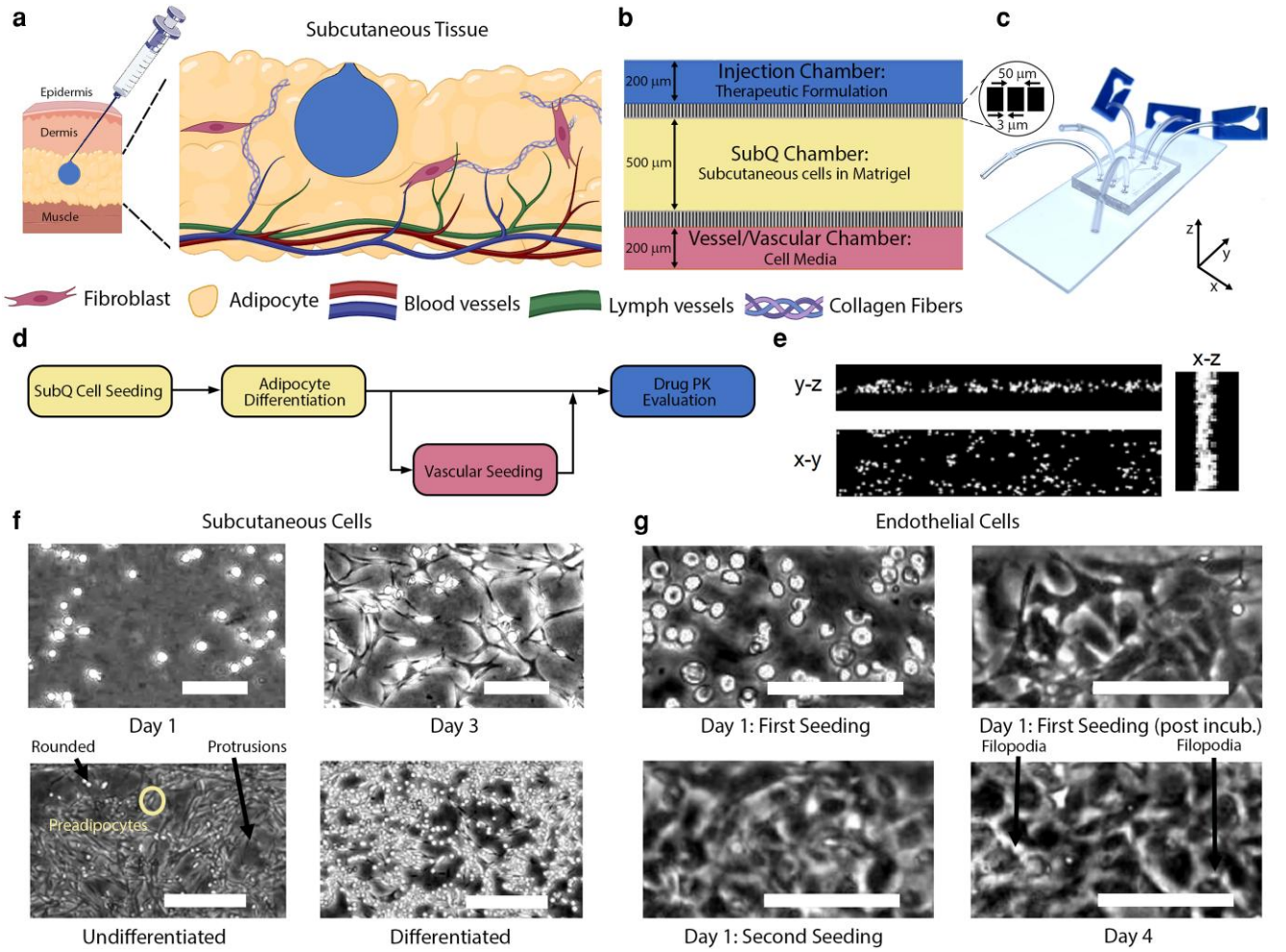

Fig. 1. a) Schematic of subQ injection and the resulting drug depot. b) A three compartment microfluidic design for mimicking drug transport following subcutaneous (subQ) injection. c) Physical microfluidic chip with tubing and clips used for the experiments. d) SubCuTIS development protocol. e) The uniformity of the initial cell distribution in the subQ channel can be seen through actin staining and confocal microscopy. f), g) The growth and expansion of mice subQ cells and endothelial cells. Scale bars: 50 μm f), 100 μm g).

SubCuTIS are similar to the nonselective pores in the lymphatic vasculature (2, 34) and have comparable permeabilities (Fig. S2). A snapshot of the complete microfluidic chip utilized in this study is shown in Fig. 1c.

Accounting for the dynamics of complex fluids and transport kinetics through porous materials (Table S1), we developed a protocol to seed and maintain multiple mice or human cells within the microfluidic chip for at least 10 days (Fig. 1d). Each step in the protocol relies solely on perfusion of various liquid mixtures through the chip compartments utilizing syringe pumps. The subQ compartment comprises a 3D coculture of fibroblasts and adipocytes in a Matrigel scaffold, initiated by injecting into the chamber a 3:1 mixture of preadipocytes and fibroblasts in cold matrigel (Fig. S3 a, b, e, f). Here, we used an intermediate perfusion rate (5 μl/min) based on two constraints: a slow rate results in cell settling and premature polymerization (35), while fluid shear at high flow rates can not only damage cells and Matrigel (36, 37), but also lead to an inhomogeneous cell distribution (Fig. S4). The device was then incubated at 37°c for the mixture to polymerize. At 37°c, the resulting gel mixture had storage (G') and loss (G") moduli similar to the ECM (38) (Fig. S5). Confocal microscopy confirmed a homogeneous initial cell distribution (Fig. 1e). To avoid damaging the subQ tissue structure, its media exchange was performed in the neighboring compartment and was mediated by the narrow slits (Fig. 1b). Preadipocytes and fibroblasts in the subQ compartment grew to confluency after 5 days, resulting in a dense 3D cellular network (39, 40) distinct from 2D cultures in flasks (Fig. 1f, Fig. S3a, b). Both preadipocytes and fibroblasts displayed more elongated shapes with fewer protrusions in 3D, consistent with previous findings (41). Instead of directly manipulating finicky adipocytes, we induced adipocyte differentiation (27, 29, 31, 32) in situ to achieve the final subQ tissue structure. We observed a morphological change of cells from elongated to a more rounded shape as previously reported (42), which may influence subQ transport both physically and biologically (Fig. 1f).

To mimic the blood capillary vessel walls, we seeded endothelial cells into the vascular compartment at a high density (1×10^7 cells/ml) twice to ensure sufficient attachment onto the channel walls and form a confluent lining (13) (Fig. 1g). We observed a 2D cell morphology similar to those in flasks (Fig. S3c) as previously reported. Asymmetric filopodia extensions indicating polarization towards a migratory endothelial phenotype were rare (36). To mimic the lymphatics which have an open and loose structure (2), we left the vessel compartment empty such that macromolecules can diffuse freely through the 3 μm slits, whose permeability is comparable to the in vivo lymphatics (Fig. S2). Finally, it is worth

noting that human subQ and endothelial cells are larger than mice cells but have similar morphologies (Fig. S3d). This size difference may influence the rates of drug transport and pharmacokinetics, which is discussed later.

SubQ tissue on a chip mimics human physiology

We evaluated the physiology of the developed in vitro subQ tissue utilizing a combination of confocal imaging assays and SEM imaging. Utilizing actin and nucleus staining with confocal microscopy, we examined the in vitro tissue structures (Fig. 2a,b). SubQ and vascular compartments display distinct cellular structures that are vital to mimicking ideal drug transport barriers: the subQ tissue spanned the entire compartment with a 3D architecture; endothelial cells formed a complete lumen with a confluent monolayer lining the inside walls, thus presenting a barrier similar to blood capillaries. We observed greater than 90% viability for both subQ cells and endothelial cells at the end of transport measurements using C12-resazurin live/dead staining (Fig. 2c–e). This validated our chip development and imaging protocols, demonstrating that our microfluidic cell culturing device is as durable as other custom-fabricated microphysiological systems for maintaining live cells (27, 28, 43).

In addition to the cellular structure, we studied the ECM surrounding subQ cells, where drug transport occurs. Scanning electron microscopy (Fig. 2f) confirmed the presence of connective tissues surrounding fat cells. These high magnification images also reveal porous microstructures within the ECM, similar to those observed in ex vivo tissue samples (44, 45). Sirius red staining shows the presence of collagen outside the cells (Fig. 2g), while the presence of hyaluronic acid was confirmed with a hyaluronic acid binding protein assay (Fig. S6). In the vascular compartment, we examined the expression of tight junction protein Claudin-5 (Fig. 2h). The presence of tight junction proteins between endothelial cells indicates the integrity of the vascular endothelial barrier (13, 43). In the subQ compartment, we confirmed the presence of intracellular lipid droplets corresponding to adipocytes using Oil Red O staining (Fig. 2i). We measured a significant increase in the lipid content after differentiation (Fig. 2j). Since adipocytes can be derived from both preadipocytes and fibroblasts (46) seeded in the chip, we also quantified their differentiations independently on plate assays, which confirmed that preadipocyte differentiation plays the dominant role in a cocultured subQ environment (Fig. S7).

SubQ tissue on a chip differentiates macromolecular transport based on MW, charge, and shape

We quantified macromolecule transport in SubCuTIS by injecting fluorescently labeled solutions into the injection chamber and acquiring time correlated image sequences lasting at least three hours utilizing a confocal microscope with an incubation chamber (Fig. 3a). The concentration of the injected solutions was restricted to 1 mg/ml, where a linear correlation exists between solute concentration and fluorescence intensity ($R^2 = 0.9954$, Fig. 3b). We also verified, utilizing gel permeation chromatography (GPC) and alternate fluorescent labeling, that the presence of a fluorophore did not significantly influence the size and transport characteristics of the tested molecules (Fig. S9). The time correlated fluorescence data were processed utilizing computationally efficient frameworks (Fig. S10 and Materials and methods section) to obtain the three key rate constants that describe concentrations in each compartment: the permeability R_{12} from the injection compartment to the subQ compartment, the diffusivity in the subQ compartment D_2 and the permeability R_{23} from the subQ channel into either the lymphatic or vascular compartment (Fig. 3a and Materials and methods section for definition of the rate constants).

To evaluate the effects of molecular weight (MW), charge and shape on the three rate constants, we performed experiments with FITC-Dextran as a model molecule (Fig. 3). We tested 10, 40, and 150 kDa dextrans to probe effects of MW, while anionic FITC-CM-dextran and cationic FITC-DEAE-dextran with matching MW (40 kDa) were evaluated to study the effects of charge. We also examined the role of molecular shape by comparing transport of IgG and dextran at matching MW (150 kDa).

Focusing on the transport from the injection compartment to the subQ compartment, we found that R_{12} was close to 10-fold lower compared to that in PBS control (Fig. S8). This reduced R_{12} confirmed that the major transport barrier for entering the subQ compartment is the actual tissue environment, instead of the narrow slits presented by the chip geometry. The resistance to enter the finely porous subQ ECM is also responsible for the inverse relationship between R_{12} and MW (Fig. 3c). For the same MW, R_{12} is highest for positively charged and lowest for negatively charged molecules (Fig. 3c). While various ECM components carry opposite charges, overall, the interstitial space is negatively charged (1). Due to electrostatic repulsion, negatively charged molecules enter the subQ space more slowly, resulting in a lower value of R_{12}. IgGs were also observed to permeate slower into the subQ chamber as compared to linear dextran molecules (Fig. 3e).

Diffusion is the major transport mechanism across the subQ compartment. We validated the developed methodology for extracting diffusion coefficients utilizing a combination of fully resolved simulations, and orthogonal localized fluorescence recovery after photo-bleaching measurements (Fig. 3f, Fig. S10). Our measured diffusion coefficient (D_2) values agree with the in vivo data for diffusion in normal tissues and show MW scaling consistent with diffusion of polymers in gels (Fig. 3g) (47, 48). Anionic molecules are observed to diffuse faster in the negatively charged subQ ECM (Fig. 3h), consistent with existing findings (49). On the contrary, IgGs that carry a weak negative charge under physiological conditions diffuse slower than linear dextrans of similar MW (Fig. 3i). Our measured subQ IgG diffusivity is consistent with previous findings for the interstitial transport of dextran and proteins at matching MW in vivo (9). The differences in diffusivity between IgGs and 150 kDa Dextran are likely due to the differences in their molecular shape, with the flexible random-coil configuration of dextran polymers enhancing their transport (50).

The well-known enhanced permeability of lymphatic systems relative to the blood vasculature is captured in our chip design (Fig. 3j). As seen from the ratio of $R_{23,\mathrm{Lymph}}/R_{23,\mathrm{Blood}}$, the lymphatic permeability was at least 4 times higher for all tested molecules and was as high as 17 times for IgGs. Probing permeabilities in the blood vasculature further, we find that $R_{23,\mathrm{Blood}}$ in the vascular compartment decays faster with MW than D_2 (Fig. 3k), which can be explained by the small size of gap junctions between endothelial cells (1 nm) (51) as compared to the relatively large pore size in the subQ tissue (~ 10–$100\ \mathrm{nm}^2$). We thus expect greater hindrance for macromolecules to cross the endothelial barrier compared to the steric hindrance experienced during subQ diffusion (1–3). Our experimental measurements of R_{23}, on the order of 10^{-3}–10^{-4} μm/s, agree with in vivo (52, 53) and in vitro measurements (54), and confirm the formation of a physiological endothelial barrier. Counteracting influence of the negative charges on the ECM and the endothelial surface is likely the reason for the charge

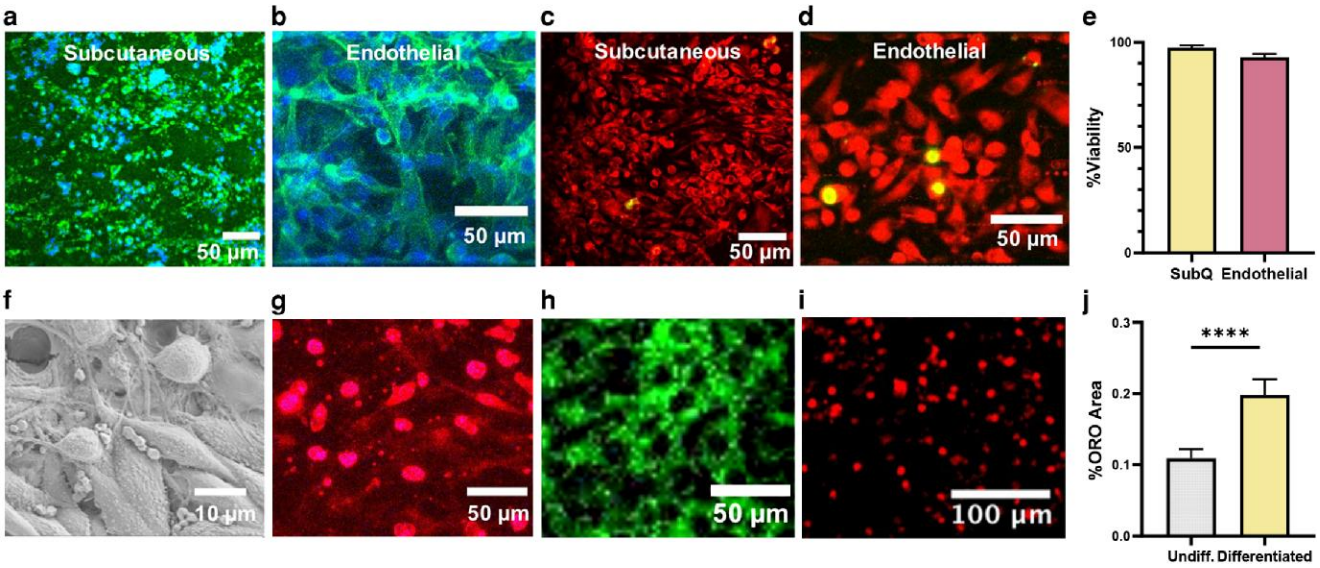

Fig. 2. a, b) Actin (green) and nucleus (blue) staining of subQ and endothelial compartment. c, d) C12 Resazurin/SYTOX Green Live (red)/dead (green) staining, and e) quantification of cell viability. SubQ and endothelial respectively denotes subQ and endothelial cells. f) SEM images of the developed subQ tissue. g) Sirius red staining of collagen in subQ cells and ECM. h) Expression of endothelial tight junction protein Claudin-5 (green) i) Oil Red O staining showing presence of lipids within the subQ tissue. j) Amount of lipids increase postadipocyte differentiation. Undiff. denotes the undifferentiated state.

independence of $R_{23,Blood}$ (Fig. 3l). Compared to linear dextrans of identical MW, IgGs are further hindered by the endothelial barrier (Fig. 3m).

The overall transport of a macromolecule is dictated by the interplay between size, charge and shape. Of these, size serves as a critical determinant due to the substantial diversity in the molecular weights of bio-macromolecules. For a fixed size, charge plays a multifaceted role in dictating transport via electrostatic interactions. For example, electrostatic repulsion hinders the permeation of anionic molecules from the drug depot into the ECM. However, permeability across the depot-ECM interface is only the first step in the transport cascade (Fig. S11). Diffusion, the primary drug transport mechanism within the ECM, is facilitated by negative charges (Fig. 3h). As a result, overall, negatively charged molecules (or less positively charged) are more effectively transported across the ECM (49). Anionic molecules are also known to be less susceptible to clearance. Bioavailability, which depends on the cumulative transport into the systemic circulation, is thus expected to be higher for negatively or less positively charged molecules (55). Finally, shape could become important for the transport of larger molecules. For instance, a globular molecule can physically be constrained by a pore smaller than its diameter, whereas a linear molecule with the same molecular weight can move through the pore under the right orientation.

SubCuTIS predicts systemic adsorption pathways and in vivo pharmacokinetics

Detailed transport characterization of subcutaneously administered drugs has been very limited due to technical difficulties associated with obtaining spatio-temporally resolved measurements of drug concentration in animal models (3). SubCuTIS overcomes these limitations and provides a convenient platform to characterize transport parameters and assess clinical bioavailability of drugs, as demonstrated by experiments with 7 clinically approved mAbs and a preclinical IgG fragment (Fig. 4). The relevant properties of the tested mAbs are presented in Table S2.

Compared to the existing one-step transport models (13), the multicompartment geometry of our chip allows us to independently characterize the rate constants associated with each transport barrier encountered by subcutaneously administered drugs. As shown in Fig. 4a–d, the three rate constants vary significantly across the tested mAbs. Interestingly, in alignment with in vivo data (10, 11), we also find that the rate constants differ across mice and human chips. Notably, the diffusion coefficients in the mice chips are relatively smaller, which is in alignment with the denser murine adipocyte packing in vivo (56). Small pore sizes resulting from dense adipocyte packing might also be the reason behind the amplified differences between R_{12} and R_{23} in mice chips. Though beyond the scope of the current study, subQ tissue chips present an opportunity to systematically understand the mechanisms responsible for the poor subQ PK correlation between humans and animal models (10, 11), and thus better interpret animal data (Fig. S12).

SubCuTIS also allows us to establish a drug's systemic absorption pathways by measuring R_{23} with and without endothelial cells. As the lymphatic and blood vasculature have approximately similar surface area per unit tissue volume (19, 57–59) and are subjected to similar drug concentration differences, the relative amount of drug entering the lymphatics can be calculated from the relative proportion of lymphatic permeability $R_{23,Lymph}$ to that of the total lymphatic and blood vasculature permeabilities (Fig. 4f). For IgGs, we observe that more than 90% of the drug permeates through the lymphatics, in alignment with the limited in vivo data available through animal models (3). We also observe that vascular transport contributes to a larger extent for systematic absorption of smaller IgG fragments (Fig. S13). This, along with the significantly higher subQ diffusivity of IgG Fragments (Fig. 4c), explains their significantly shorter adsorption time (Table S2).

The three rate constants also allow us to obtain local adsorption rates within the subQ tissue (Fig. 4g). Assuming a spherical drug depot after injection, drug transport across the tissue can be modeled with a 1D diffusion equation with a sink term scaling

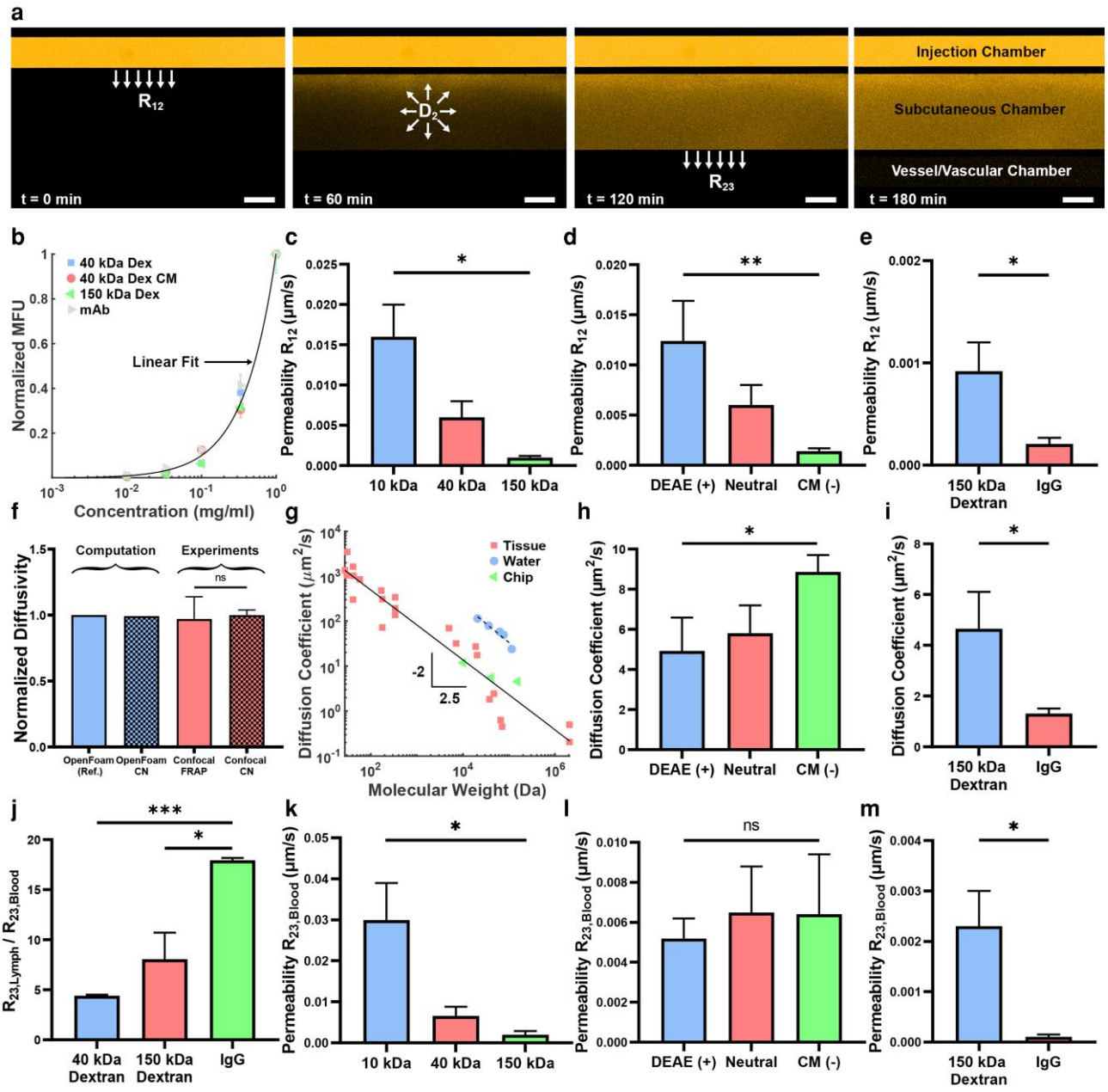

Fig. 3. SubCuTIS differentiates the transport of macromolecules based on their size, charge, and shape. a) Time correlated fluorescence microscopy images (false colored) showing the macromolecule transport and the rate constants within the chip. b) Fluorescence intensity of tested macromolecules are linear at concentrations at or below 1 *mg/ml*. c–e) Effect of MW, charge and size respectively on R_{12}. f) Validation of diffusion coefficient extraction through fully resolved simulations and FRAP. g–i) Effect of MW, charge and size on respectively D_2. j) Relative permeability across blood and lymphatic vasculature for common macromolecules. k–m) Effect of MW, charge and size respectively on blood vasculature permeability $R_{23,Blood}$.

with $R_{23,Lymph}$ (60), subject to a Neumann influx boundary condition scaling with R_{12} (Fig. S14). The two relevant first-order adsorption rate constants—rate at which the drug enters the subQ tissue from the drug depot $k_{abs,in}$ and rate at which the drug leaves the subQ tissue $k_{abs,out}$—can be recovered by integrating and fitting the spatio-temporal drug concentration obtained from the 1D diffusion equation to a single exponential (Fig. 4g). Comparing $k_{abs,in}$ and $k_{abs,out}$ allows us to establish the rate limiting transport step in drug adsorption. When $k_{abs,out} \approx k_{abs,in}$, such as in the case of mAb 5, drug adsorption is throttled by the influx from the depot. On the other hand, when $k_{abs,out} < k_{abs,in}$, such as the case of mAb 3, adsorption is limited by the transport within the subQ tissue. In this case, the drug spends a relatively higher amount of time within the subQ ECM making it vulnerable to increased proteolytic degradation (catabolism), and consequently affecting the bioavailability of the drug.

BA depends on the fraction of drug absorbed into the blood stream, which in turn is dictated by the amount of drug eliminated at the injection site. Proteolytic catabolism is a major source of mAb degradation and elimination (61, 62), and is known to obey first order kinetics (63, 64). Integrating first-order catabolic loss into the previously detailed subQ transport model, we find theoretically that bioavailability scales as $k_{abs,out}/(k_{abs,out} + k_{cat})$, where k_{cat} is the catabolic elimination rate constant (Fig. S15). Unlike linear correlations previously reported in literature for interpreting data from acellular in vitro models (13), the above scaling is

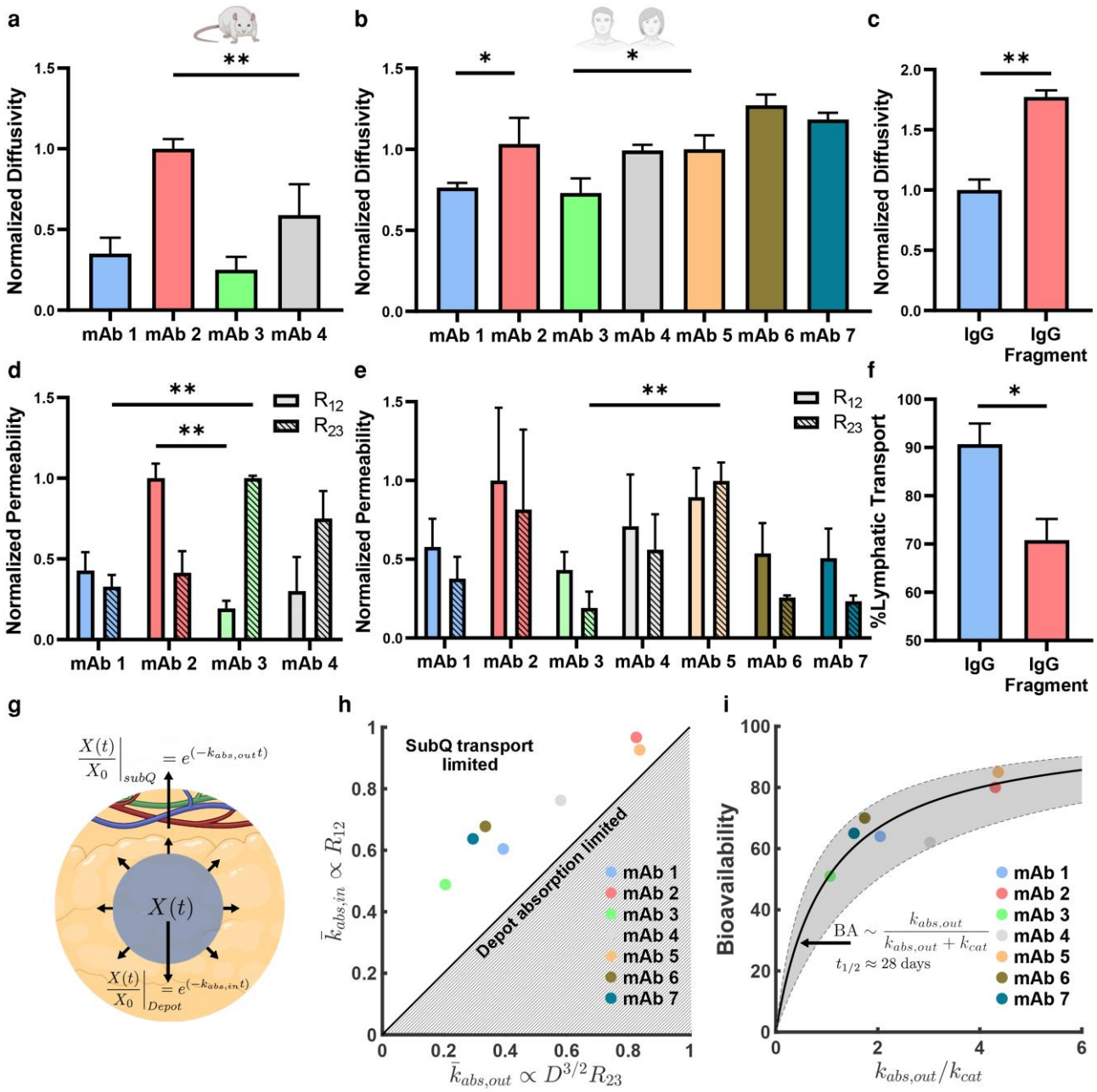

Fig. 4. SubCuTIS is effective for quantifying local subQ absorption rate constants and for assessing clinical bioavailability. a, b) Normalized diffusivity of mAbs in mice and human chips, respectively. c) IgG fragments diffuse significantly faster as compared to an intact IgG (mAb 5 shown). d, e) Permeabilities R_{12} and $R_{23,Lymph}$ (lymphatic) of mAbs in mice and human chips, respectively. The permeabilities are normalized with the largest value obtained within a chip, which is mAb 2 R_{12} for both mice and human chips. f) A relatively larger fraction of IgG fragments enter systemic circulation via the blood vasculature. g) Schematic illustrating the definition of the local first-order absorption rate constants $k_{abs,in}$ and $k_{abs,out}$. $k_{abs,in}$ physically captures the rate at which the drug enters the subQ tissue from the depot and is evaluated by fitting the evolution of drug concentration within the depot to a single exponential (first-order kinetics). $k_{abs,out}$ captures the rate at which the drug leaves the subQ tissue, and is evaluated by fitting the evolution of drug concentration within the entire subQ volume to a single exponential. h) The correlation plot between the obtained rate constants reveals the rate limiting step in local subQ transport of the tested mAbs. i) The bioavailability of mAbs is dictated by the competition between the local absorption rate and proteolytic catabolism rate constant (k_{cat}) as $BA \sim k_{abs,out}/(k_{abs,out} + k_{cat})$. mAbs 5 and 7 have nonlinear PK. The shaded region indicates the uncertainty in assessed BA.

bounded between 0 and 1 (in alignment with the definition of bioavailability) for all physically possible values of the local rate constants. The theoretical scaling assuming a fixed value of k_{cat} is shown as the solid black line in Fig. 4i. The best fit value of k_{cat} corresponds to a value of $t_{1/2} \approx 28$ days, which is within the range of half lives expected for mAbs (65). The shaded region indicates the uncertainty in calculation of bioavailability due to expected variability in adipose and lymphatic density in the subQ tissue (Fig. S15). The average uncertainty in BA is about 18, which is comparable to BA reported from clinical trials (10). It is worth noting, as expected (55), simple metrics such as aggregate molecular charge in isolation are insufficient to predict the transport rate constants or BA (Fig. S16). Overall, the excellent agreement between theoretical scaling and experiments provides a sound and

convenient basis to infer BA by measuring $k_{abs,out}$ utilizing SubCuTIS.

Discussion

SubQ transport is a slow process due to interactions between complex drug macromolecules and the heterogeneous tissue environment. The emergent time scales of drug transport dictate important pharmacokinetic (PK) parameters like bioavailability. Existing in vivo models are inconvenient to use and are poor predictors of human PK characteristics, while existing in vitro models are acellular and do not accurately mimic the subQ tissue physiology. Facile and accurate evaluation of drug transport thus requires a high fidelity in vitro drug testing platform for subQ injections, which has been challenging to develop due to the difficulty in manipulating mature adipose cells, maintaining cells at high confluency, and accurately modeling the endothelial lumen. Overcoming such challenges using microfluidics requires substantial modifications to existing cell culturing protocols.

Here, we demonstrate the development and utility of a facile *Sub*cutaneous Co-*C*ulture *T*issue-on-a-chip for *I*njection Simulation (SubCuTIS) constructed utilizing a simple commercially available three-compartment microfluidic platform. We highlighted the importance of controlling the perfusion rates, cell-Matrigel suspension rheology, the initial cell distribution and reagent concentrations for mass transfer that are often overlooked but are crucial for capturing in vivo physiology. We also demonstrated the flexibility of the developed chip to simulate both human and animal subQ tissues. We performed controlled experiments with model Dextran molecules and established in vivo like sensitivity of the chip to changes in macromolecule molecular weight, charge and shape. Evaluating the transport characteristics of clinically available mAbs with diverse bioavailabilities on a human SubCuTIS revealed statistically significant differences in their transport, including their diffusivity in the subQ tissue and permeability across biological barriers. By comparing the relative permeability across lymphatic and vascular barriers, we demonstrated the ability of the chip to predict the systemic pathways for drug absorption. We mathematically linked the macromolecule diffusivity and permeabilities to two key local absorption rate constants dictating respectively the rate of drug permeation into the tissue from the injection site $k_{abs,in}$, and the rate of drug entering the systemic circulation $k_{abs,out}$. Finally, accounting for the first-order kinetics of proteolytic elimination, we established a theoretical link between the measurable $k_{abs,out}$ and the bioavailability of the drug. The ability to comprehensively characterize the local absorption rates through the subQ chip thus opens up opportunities to systematically formulate drugs with desired PK characteristics.

Notably, our chip does not simulate poroelastic convective transport of subcutaneously administrated drugs (16). The time scales associated with significant subQ convection span a few seconds, aligning closely with the injection duration (15, 16, 66). On the other hand, subQ pharmacokinetics are characterized by much longer time scales spanning several days. This fact, along with the analysis presented in Fig. S17 and the good prediction of bioavailability from the transport coefficients measured from our chip (Fig. 4i) suggest that diffusive processes play a dominant role in subQ pharmacokinetics. Nevertheless, future studies should systematically probe and confirm the influence of convection.

There remain several other opportunities for future work that would offer important extensions to the present work. In comparison to subQ chips with human cells, mAb transport in mice chips showed differences in all measured transport coefficients, similar to differences in in vivo mAb PK characteristics in mice and humans. SubQ tissue chips thus present an opportunity to systematically understand the mechanisms responsible for the poor correlation between human and mice PK characteristics and enable better interpretation of murine PK data. The existing chip design avoided the use of lymphatic endothelial cells; incorporating these cells could make the chip more physiological and might further improve bioavailability prediction. Further, mAbs had negligible irreversible binding at the tested concentrations in the subQ space (Fig. S18). Although mAb binding is expected to decrease all three measured rate constants and lead to an expected loss in bioavailability, it is important for future studies to confirm this across a wide range of mAb concentrations that are representative of clinical doses. Future studies could also evaluate permeates from the microfluidic device with GPC, analytical methods, or in vitro assays, such as ELISA, for more in-depth analysis of the transported drug. Overall, this technology represents a powerful new platform that uses commercial microfluidic chips and automated data quantification methods as a standardized assay for high-throughput testing and selection of mAb drug candidates with beneficial pharmacokinetics. We believe that this technology increases the versatility of organs-on-chips with broad applications in drug discovery and formulation designs, and beyond.

Materials and methods

Microfluidic device and processing

Microfluidic chips with three-compartment designs were purchased from SynVivo, Inc. (catalog #108011). The basic device setup and manipulation follow manufacturer instructions (downloadable at synvivobio.com). In brief, each inlet or outlet port was connected to a Tygon ND-100-80 non-DEHP medical tubing (Saint-Gobain). and closed using clamps (catalog #202003, Synvivo, Inc.) prior to priming and incubation. During liquid exchange, clamps were removed. Flow in each compartment was individually controlled by connecting the corresponding inlet tubing to a 24" Jensen global dispensing needle (TestEquity LLC) on a 1 ml luer lock syringe (BD biosciences). Flow rates were controlled by mounting the syringe on a programmable syringe pump (Harvard Apparatus). Outlet tubings were connected to waste collecting tubes.

Liquid exchange procedures were performed under a microscope with a 4X objective to monitor cell growth and detect bubble formation in real time. To prevent contamination, the inlet tubing was replaced during each liquid exchange step. A drop of sterile water was placed around the inlet port before the removal of old tubing to seal the port. A new tubing containing fresh liquid was then inserted into the inlet port. Unless noted otherwise, each liquid exchange step was performed as a brief perfusion in the specified channel and lasted for no more than 5 minutes to ensure cell viability outside the incubator. Most liquid exchange steps were stopped when three drops of liquid were collected from the outlet, which ensures a complete replacement of existing liquid in the channel. For simplicity, all perfusion procedures in the injection channel were performed at 10 μl/min. All perfusion procedures in the vascular channel were performed at 2 μl/min unless specified otherwise (Table S1).

Microfluidic cell culture

Mice subQ fibroblasts (L, ATCC), mice subQ preadipocytes (X9, ATCC), mice aortic endothelial cells (MAOEC, iXCells), human

subQ preadipocytes (PCS-210-010, ATCC), human dermal fibroblasts (NHDF, C-12302, PromoCell), human endothelial cells (EA.hy926, ATCC) were obtained from commercial suppliers. To maintain cells in tissue culture flasks, we used DMEM (ATCC) supplemented with 10% FBS for endothelial cells, DMEM/F12 (ATCC) supplemented with 15% FBS for mice preadipocytes and fibroblasts, fibroblast basal medium with low-serum growth kit (ATCC) for human preadipocytes and fibroblasts. Unless noted otherwise, all incubation steps in tissue culture flasks and chips were performed at 37°C, 5% CO_2 and 85 ~ 90% humidity. For microfluidic cell cultures, passage numbers between 6 and 15 were used.

Prior to seeding cells into microfluidic channels, serum-free medium (DMEM/F12 for mice and fibroblast basal medium for human) was injected slowly into each channel. Bubbles were removed by priming i.e. by connecting one inlet port to a Pneumatic Primer (catalog #205001, Synvivo, Inc.) at 5 psi for at least 40 minutes. Bubble-free chips were cooled at 2 ~ 4°C prior to use. Matrigel (catalog #356230, Corning) was thawed on ice bath for at least 90 minutes.

For subQ seeding, preadipocytes and fibroblasts were trypsinized, resuspended in serum-free medium at 4×10^6 cells/ml and 6×10^6 cells/ml respectively for mice and human chips, and cooled on ice for 1 minute. Preadipocyte suspension, fibroblast suspension and Matrigel were mixed on ice at a 3:1:4 volumetric ratio using a precooled pipette. This mixture was quickly injected to the central subQ compartment at 5 μl/min and incubated for 90 minutes. To avoid cell sedimentation, each chip was placed in an upright position with either the inlet or outlet side lifted. After complete polymerization of Matrigel, the injection and vessel channels were perfused with full subQ culture medium at 10 μl/min. This media exchange was repeated daily for at least 7 days.

After cells reached confluency in the subQ channel, adipocyte differentiation was induced by perfusing differentiation medium into the injection compartment daily for three days. The differentiation medium contains full subQ cell culture medium supplemented with 5 μM dexamethasone, 5 mM methylisobutylxanthine and 100 μg/ml insulin. These supplements were used at higher concentrations than established protocols (67) to account for their low partitioning into the subQ compartment. After differentiation, cells were maintained using full subQ cell culture medium with 10 μg/ml insulin for daily media exchange.

Prior to seeding endothelial cells, 200 μg/ml human fibronectin in PBS was perfused into the vessel channel. The device was then incubated for at least 45 minutes and the vessel channel was washed with endothelial culture medium at 10 μl/min. Confluent endothelial cells were trypsinized from culture flasks, resuspended in endothelial culture medium at 2×10^7 cells/ml and seeded into the vessel channel at 5 μl/min. The chip was then incubated for 90 minutes with top side down to promote adhesion to the top surface. Unadhered cells were washed by endothelial culture medium. The seeding procedure was repeated using endothelial cells trypsinized from a second culture flask. After incubation with a normal chip placement for at least 4 hours, excess cells were washed by endothelial culture medium. Daily media exchange was performed using endothelial culture medium (20% FBS for mice) at 2 μl/min.

SubQ tissue characterization

After transport measurements, either fresh media (live staining) or PBS (fixation) was perfused to the injection chamber and the vessel chamber to remove fluorescence from the injected solution and incubated for 1 hour followed by a second wash. Cell viability was assessed using the live/dead cell vitality assay kit (ThermoFisher): 100 nM of Sytox green and 5 μM of C12-resazurin were injected into the injection chamber. 10 nM of Sytox green and 500 nM of C12-resazurin were injected into the endothelial chamber. The device was incubated again for 1 hour, washed with fresh media, incubated for 30 minutes and washed again for imaging. For other staining assays, 16% PFA (injection chamber) and 4% PFA (the 435 vascular chamber) were first perfused into the device for cell fixation, followed by a 1-hour fixation and a second wash for 30 minutes. 1.0% Triton X-100 in PBS (injection chamber) and 0.2% Triton X-100 in PBS (the vascular chamber) were then perfused into the device for cell permeabilization, followed by a 1-hour fixation and a second wash for 30 minutes. Various staining markers were applied to the device and incubated for 1–3 hours (Table S3), washed with PBS, incubated for 30 minutes, washed again and was ready for imaging. Z-stacks of images were taken for live and fixed cells using an inverted confocal microscope (Zeiss LSM 710) with 10X and 32X water immersion objectives. Image processing and 3D z-stack reconstruction were performed using ImageJ software.

Rheological characterization

AR-G2 rheometer (TA instruments) with a 40-mm-diameter, 2° cone and plate geometry were used to measure the rheological properties of pure Matrigel and Matrigel:medium mixture. The mixture sample was prepared by mixing 50% thawed Matrigel and 50% precooled DMEM/F12 on an ice bath. For frequency sweeps, the shear storage (G′) and loss (G″) moduli were measured at an oscillatory strain of 0.1, which is below the maximum strain amplitude in the linear response regime (68). For flow sweeps, the viscosity was measured with increasing and decreasing shear rates. For each type of measurement, the temperature effects were investigated in two ways. For a fixed temperature, we set the rheometer temperature to 37°C followed by an equilibration for 2 minutes. Measurements were taken immediately after loading the cold sample and repeated for 1 hour until the sample was fully polymerized. For an increasing temperature, the rheometer was cooled to 2°C and equilibrated for 2 minutes before samples were loaded. Measurements were repeated at increasing temperatures until 37°C with 1 minute equilibration between each temperature.

Scanning electron microscopy

Fixed cells were dehydrated by gently adding ethanol at increasing percentages in DI water (50%, 70%, 80% twice, 90% twice and 100% twice), with 20 minutes between each wash. Samples were then transferred to the Center for Nanoscale Systems for further preparation and imaging.

Gel permeation chromatography

The molecular size distributions of mAb solutions were characterized using a GPC System equipped with a TDA 305 triple detector (Viscotek TDAmax, Malvern, UK). Mab solutions were collected from the microfluidic device by perfusion with air in the injection and vascular compartments. Samples were purified using 4 mm syringe filters and injected with a flow rate of 0.75 ml/min for 30 min. The UV detector was set with 280 nm wavelength. TSK-GEL G3000SWXL (Tosoh Corporation, Tokyo, Japan) was used. The mobile phase was PBS with Ca++ and Mg++.

Fluorescent labeling of antibodies

Monoclonal antibodies (mAbs) were labeled with FITC (ex/em 494/518 nm) and Rhodamine-RedX (ex/em 560/580 nm) by respectively incubating the mAbs with NSH-Fluorescein (ThermoFisher # 46409) and Rhodamine Red™-X, Succinimidyl Ester (Invitrogen # R6160) in freshly prepared reaction buffers as per supplier recommendations. After the reaction, excess unreacted fluorophores were removed by desalting the samples in PBS (pH 7.4) using 40 MWCO Zeba spin desalting columns (Thermo Scientific # 87769).

Macromolecule transport measurements

Transport measurement and calculation. FITC-dextran (MW 10 kDa, 40 kDa and 150 kDa), FITC-DEAE-dextran (40 kDa) and FITC-CM-dextran (40 kDa) were obtained from Sigma Aldrich. FITC-dextran is neutral while 40 kDa FITC-DEAE-dextran has a zeta potential of 8.178 ± 1.421 mV and 40 kDa FITC-CM-dextran has a zeta potential of −13.8 ± 2.221 mV. Mouse FITC-IgG was obtained from Southern Biotechnology Associates. Rhodamine and FITC-labeled therapeutic mAbs were provided by Sanofi. Acquisition of images for transport measurement were performed using an inverted microscope (Axio Observer Z1, Zeiss for mice chips and LSM 900, Zeiss for human chips) with an incubator chamber (Zeiss) to maintain 37°C, 5% CO_2 and controlled humidity for live cell imaging. Prior to each experiment, the injection compartment of linear chips was washed with PBS and perfused with macromolecular solutions. Images were acquired at 1-minute intervals for 3 to 6 hours, except control experiments without cells (30-second intervals for 2 hours).

Calculation of rate constants

To mitigate the need for costly numerical simulation and simplify the calculation of rate constants, we consider a 1D transport problem in the linear chips. This approximation is justified as the span of the linear chip (y-direction in Fig. 1c) exceeds the primary transport direction (x) by a factor larger than 10.

Based on Fick's law of diffusion, the apparent permeability ($R^0_{\alpha\beta}$) across any two chambers α and β can be written as $R^0_{\alpha\beta} = \frac{1}{A\Delta C_{\alpha\beta}}\frac{dQ_{\alpha\beta}}{dt}$ (69), where A is the cross area available for transport, $\Delta C_{\alpha\beta}$ the concentration difference across the chambers and $Q_{\alpha\beta}$ is the total amount of transported permeant. We used $C_{12} \approx C_1$ ($C_1(t) \gg C_2(x, t)\ \forall t$), and $C_{23} = C_2 - C_3$, and estimated R_{12} and R_{23} when Q_{12} (total permeant in subQ and vessel compartments) Q_{23} respectively grew linearly with time (Fig. S10). The actual tissue/vascular permeability $R_{\alpha\beta}$ can be recovered by discounting the slit permeability as $\frac{1}{R_{\alpha\beta}} = \frac{1}{R^0_{\alpha\beta}} - \frac{1}{R_{slit}}$. R_{slit} was calculated utilizing Dextran permeation experiments in chips filled with PBS (Fig. S2). It is important to note that permeability is distinct from the diffusion coefficient even though both are obtained from the Ficks law. Permeability coefficients encode additional information of the interface characteristics such as the relative pore size and interface charge (70, 71), both of which play a crucial role in dictating the transport of drugs from one chamber to the other.

Diffusion in the subQ compartment is governed by the 1D diffusion equation $\frac{\partial C_2}{\partial t} = D_2\frac{\partial^2 C_2}{\partial x^2}$. The solution adjusted for the chip geometry and the presence of slips is $C_2(x, t) = C_0\left(1 - \frac{1}{2}\mathrm{erf}\left(\frac{\epsilon+x}{\sqrt{4D_2(t+\Delta t)}}\right) - \frac{1}{2}\mathrm{erf}\left(\frac{\tau-(\epsilon+x)}{\sqrt{4D_2(t+\Delta t)}}\right)\right)$. The five fitting parameters (D_2, Δt, τ, ϵ, and C_0) were recovered via nonlinear least square curve fitting to the experiment data using MATLAB. We orthogonally validated the diffusion coefficient extraction by (a) nonlinear least square curve fitting of experiment data to the numerical solution of 1D diffusion equation (without fitting parameters) utilizing the Crank–Nicolson method, and (b) Fluorescence Recovery After Photobleaching experiments (FRAP) (Fig. S10).

Statistical analysis

Data in all plots are expressed as mean ± s.e.m of three or more independent measurements. Statistical analysis was done in MATLAB and GraphPad Prism, and statistical significance was attributed to values of $P < 0.05$ as determined by unpaired Student's t-test, as described in the figure legends. Different significance levels (P values) are indicated in each figure with asterisks: $^*P < 0.05$, $^{**}P < 0.01$, $^{***}P < 0.005$, $^{****}P < 0.001$.

Acknowledgments

We thank Sanofi for providing the mAbs reported in the study and for the financial support. SM also acknowledges support from John A Paulson School of Engineering & Applied Sciences, Harvard University, and the Wyss Institute for Biologically Inspired Engineering. We acknowledge the use of https://www.biorender.com in creating schematics.

Supplementary Material

Supplementary material is available at *PNAS Nexus* online.

Author Contributions

V.C.S., Q.M.Q., J.Z., A.D., S.H., Y.R.G., and S.M. developed the scientific questions and hypotheses of the study; V.C.S., Q.M.Q., and S.M. designed the experiments; K.H. synthesized the fluorescently tagged mAbs; V.C.S., Q.M.Q., S.S., S.P., and N.K. conducted the experiments; V.C.S. and Q.M.Q. analyzed the results; V.C.S., Q.M.Q. and S.M. wrote the paper with the help of all authors.

Data Availability

All relevant data are included in the manuscript or supporting information.

References

1 Viola M, *et al.* 2018. Subcutaneous delivery of monoclonal antibodies: how do we get there? *J Control Release*. 286:301–314.
2 Porter CJH, Charman SA. 2000. Lymphatic transport of proteins after subcutaneous administration. *J Pharm Sci*. 89(3):297–310.
3 McLennan DN, Porter CJH, Charman SA. 2005. Subcutaneous drug delivery and the role of the lymphatics. *Drug Discov Today Technol*. 2(1):89–96.
4 Turner MR, Balu-Iyer SV. 2018. Challenges and opportunities for the subcutaneous delivery of therapeutic proteins. *J Pharm Sci*. 107(5):1247–1260.
5 Corre J, *et al.* 2006. Human subcutaneous adipose cells support complete differentiation but not self-renewal of hematopoietic progenitors. *J Cell Physiol*. 208(2):282–288.
6 Driskell RR, Jahoda CAB, Chuong C-M, Watt FM, Horsley V. 2014. Defining dermal adipose tissue. *Exp Dermatol*. 23(9):629–631.
7 Sánchez-Félix M, Burke M, Chen HH, Patterson C, Mittal S. 2020. Predicting bioavailability of monoclonal antibodies after subcutaneous administration: open innovation challenge. *Adv Drug Deliv Rev*. 167:66–77.
8 Flessner MF, Lofthouse J, Zakaria ER. 1997. In vivo diffusion of immunoglobulin g in muscle: effects of binding, solute exclusion,

and lymphatic removal. *Am J Physiol Heart Circ Physiol*. 273(6): H2783–H2793.
9 Reddy ST, Berk DA, Jain RK, Swartz MA. 2006. A sensitive in vivo model for quantifying interstitial convective transport of injected macromolecules and nanoparticles. *J Appl Physiol Respir Environ Exerc Physiol*. 101(4):1162–1169.
10 McDonald TA, Zepeda ML, Tomlinson MJ, Bee WH, Ivens IA. 2010. Subcutaneous administration of biotherapeutics: current experience in animal models. *Curr Opin Mol Ther*. 12(4):461–70.
11 Richter WF, Jacobsen B. 2014. Subcutaneous absorption of biotherapeutics: knowns and unknowns. *Drug Metab Dispos*. 42(11): 1881–1889.
12 Kinnunen HM, *et al.* 2015. A novel in vitro method to model the fate of subcutaneously administered biopharmaceuticals and associated formulation components. *J Control Release*. 214:94–102.
13 Bown HK, *et al.* 2018. In vitro model for predicting bioavailability of subcutaneously injected monoclonal antibodies. *J Control Release*. 273:13–20.
14 Lou H, Berkland C, Hageman MJ. 2021. Simulating particle movement inside subcutaneous injection site simulator (scissor) using monte-carlo method. *Int J Pharm*. 605:120824.
15 de Lucio M, *et al.* 2023. Modeling large-volume subcutaneous injection of monoclonal antibodies with anisotropic porohyperelastic models and data-driven tissue layer geometries. *J Mech Behav Biomed Mater*. 138:105602.
16 Hou P, Zheng F, Corpstein CD, Xing L, Li T. 2021. Multiphysics modeling and simulation of subcutaneous injection and absorption of biotherapeutics: sensitivity analysis. *Pharm Res*. 38(6): 1011–1030.
17 Rahimi E, Gomez H, Ardekani AM. 2022. Transport and distribution of biotherapeutics in different tissue layers after subcutaneous injection. *Int J Pharm*. 626:122125.
18 Han D, Rahimi E, Aramideh S, Ardekani AM. 2022. Transport and lymphatic uptake of biotherapeutics through subcutaneous injection. *J Pharm Sci*. 111(3):752–768.
19 Han D, *et al.* 2023. Lymphatic uptake of biotherapeutics through a 3D hybrid discrete-continuum vessel network in the skin tissue. *J Control Release*. 354:869–888.
20 Paul R. 2022. S.5002 - 117th congress (2021-2022): FDA modernization act 2.0.
21 Herland A, *et al.* 2020. Quantitative prediction of human pharmacokinetic responses to drugs via fluidically coupled vascularized organ chips. *Nat Biomed Eng*. 4(4):421–436.
22 Ronaldson-Bouchard K, *et al.* 2022. A multi-organ chip with matured tissue niches linked by vascular flow. *Nat Biomed Eng*. 6(4):351–371.
23 von Erlach T, *et al.* 2020. Robotically handled whole-tissue culture system for the screening of oral drug formulations. *Nat Biomed Eng*. 4(5):544–559.
24 Bhatia SN, Ingber DE. 2014. Microfluidic organs-on-chips. *Nat Biotechnol*. 32(8):760–772.
25 Shin Y, *et al.* 2012. Microfluidic assay for simultaneous culture of multiple cell types on surfaces or within hydrogels. *Nat Protoc*. 7(7):1247–1259.
26 Sung JH, Kam C, Shuler ML. 2010. A microfluidic device for a pharmacokinetic–pharmacodynamic (PK–PD) model on a chip. *Lab Chip*. 10(4):446–455.
27 Loskill P, *et al.* 2017. Wat-on-a-chip: a physiologically relevant microfluidic system incorporating white adipose tissue. *Lab Chip*. 17(9):1645–1654.
28 Rogal J, *et al.* 2020. Wat-on-a-chip integrating human mature white adipocytes for mechanistic research and pharmaceutical applications. *Sci Rep*. 10(1):1–12.
29 Kongsuphol P, *et al.* 2019. In vitro micro-physiological model of the inflamed human adipose tissue for immune-metabolic analysis in type II diabetes. *Sci Rep*. 9(1):1–14.
30 Tanataweethum N, *et al.* 2018. Establishment and characterization of a primary murine adipose tissue-chip. *Biotechnol Bioeng*. 115(8):1979–1987.
31 Li X, Easley CJ. 2018. Microfluidic systems for studying dynamic function of adipocytes and adipose tissue. *Anal Bioanal Chem*. 410(3):791–800.
32 Abbott RD, *et al.* 2015. Long term perfusion system supporting adipogenesis. *Methods*. 84:84–89.
33 Jain SM, Pandey K, Lahoti A, Rao PK. 2013. Evaluation of skin and subcutaneous tissue thickness at insulin injection sites in Indian, insulin naïve, type-2 diabetic adult population. *Indian J Endocrinol Metab*. 17(5):864.
34 Scallan J, Huxley V. 2009. *Capillary fluid exchange: regulation, functions, and pathology*. Colloquium Series on Integrated Systems Physiology. Morgan & Claypool Publishers.
35 Kim L, Toh Y-C, Voldman J, Yu H. 2007. A practical guide to microfluidic perfusion culture of adherent mammalian cells. *Lab Chip*. 7(6):681–694.
36 Shamloo A, Ma N, Poo MM, Sohn LL, Heilshorn SC. 2008. Endothelial cell polarization and chemotaxis in a microfluidic device. *Lab Chip*. 8(8):1292–1299.
37 Bruzewicz DA, McGuigan AP, Whitesides GM. 2008. Fabrication of a modular tissue construct in a microfluidic chip. *Lab Chip*. 8(5):663–671.
38 Kane KIW, *et al.* 2018. Determination of the rheological properties of Matrigel for optimum seeding conditions in microfluidic cell cultures. *AIP Adv*. 8(12):125332.
39 Chun T-H, Inoue M. 2014. 3-D adipocyte differentiation and periadipocyte collagen turnover. In: MacDougald Ormond A, editors. *Methods in enzymology*. Cambridge (MA): Academic Press. p. 538.
40 Sung KE, *et al.* 2013. Understanding the impact of 2D and 3D fibroblast cultures on in vitro breast cancer models. *PLoS One*. 8(10):e76373.
41 Hakkinen KM, Harunaga JS, Doyle AD, Yamada KM. 2011. Direct comparisons of the morphology, migration, cell adhesions, and actin cytoskeleton of fibroblasts in four different 3D extracellular matrices. *Tissue Eng Part A*. 17(5-6):713–724.
42 Lai N, Sims JK, Jeon NL, Lee K. 2012. Adipocyte induction of preadipocyte differentiation in a gradient chamber. *Tissue Eng Part C: Methods*. 18(12):958–967.
43 Adriani G, Ma D, Pavesi A, Kamm RD, Goh ELK. 2017. A 3D neurovascular microfluidic model consisting of neurons, astrocytes and cerebral endothelial cells as a blood–brain barrier. *Lab Chip*. 17(3):448–459.
44 Sbarbati A. 2010. Subcutaneous adipose tissue classification. *Eur J Histochem: EJH*. 54(4):226–230.
45 Panettiere P. 2011. The trochanteric fat pad. *Eur J Histochem: EJH*. 55(2):85–89.
46 Chang Y, *et al.* 2016. Multiple directional differentiation difference of neonatal rat fibroblasts from six organs. *Cell Physiol Biochem*. 39(1):157–171.
47 Swabb EA, Wei J, Gullino PM. 1974. Diffusion and convection in normal and neoplastic tissues. *Cancer Res*. 34(10):2814–2822.
48 Yuan W, Lv Y, Zeng M, Fu BM. 2009. Non-invasive measurement of solute permeability in cerebral microvessels of the rat. *Microvasc Res*. 77(2):166–173.
49 Arends F, *et al.* 2015. A microfluidics approach to study the accumulation of molecules at basal lamina interfaces. *Lab Chip*. 15(16):3326–3334.

50 Venturoli D, Rippe B. 2005. Ficoll and dextran vs. globular proteins as probes for testing glomerular permselectivity: effects of molecular size, shape, charge, and deformability. *Am J Physiol-Renal Physiol*. 288(4):F605–F613.

51 Feine I, Pinkas I, Salomon Y, Scherz A. 2012. Local oxidative stress expansion through endothelial cells–a key role for gap junction intercellular communication. *PLoS One*. 7(7):e41633.

52 Sato M, *et al*. 2015. Microcirculation-on-a-chip: a microfluidic platform for assaying blood-and lymphatic-vessel permeability. *PLoS One*. 10(9):e0137301.

53 Bischoff I, *et al*. 2016. Pitfalls in assessing microvascular endothelial barrier function: impedance-based devices versus the classic macromolecular tracer assay. *Sci Rep*. 6(1):1–11.

54 Offeddu GS. 2022. Microphysiological endothelial models to characterize subcutaneous drug absorption. *ALTEX-Altern Anim Ex*. 40(2):299–313.

55 Datta-Mannan A, *et al*. 2020. Influence of physiochemical properties on the subcutaneous absorption and bioavailability of monoclonal antibodies. *MAbs*. 12(1):1770028.

56 Blackshear CP, *et al*. 2018. Utilizing confocal microscopy to characterize human and mouse adipose tissue. *Tissue Eng Part C Methods*. 24(10):566–577.

57 Roose T, Swartz MA. 2012. Multiscale modeling of lymphatic drainage from tissues using homogenization theory. *J Biomech*. 45(1):107–115.

58 Gersh I, Still MA. 1945. Blood vessels in fat tissue. Relation to problems of gas exchange. *J Exp Med*. 81(2):219–232.

59 Jain RK, Tong RT, Munn LL. 2007. Effect of vascular normalization by antiangiogenic therapy on interstitial hypertension, peritumor edema, and lymphatic metastasis: insights from a mathematical model. *Cancer Res*. 67(6):2729–2735.

60 Zheng F, Hou P, Corpstein CD, Park K, Li T. 2021. Multiscale pharmacokinetic modeling of systemic exposure of subcutaneously injected biotherapeutics. *J Control Release*. 337:407–416.

61 Esposito S, *et al*. 2018. A liquid chromatography high-resolution mass spectrometry in vitro assay to assess metabolism at the injection site of subcutaneously administered therapeutic peptides. *J Pharm Biomed Anal*. 159:449–458.

62 Li B, *et al*. 2014. Framework selection can influence pharmacokinetics of a humanized therapeutic antibody through differences in molecule charge. *MAbs*. 6(5):1255–1264.

63 Brambell FWR, Hemmings WA, Morris IG. 1964. A theoretical model of γ-globulin catabolism. *Nature*. 203(4952):1352–1355.

64 Garg A, Balthasar JP. 2007. Physiologically-based pharmacokinetic (PBPK) model to predict IgG tissue kinetics in wild-type and FcRn-knockout mice. *J Pharmacokinet Pharmacodyn*. 34:687–709.

65 Keizer RJ, Huitema ADR, Schellens JHM, Beijnen JH. 2010. Clinical pharmacokinetics of therapeutic monoclonal antibodies. *Clin Pharmacokinet*. 49(8):493–507.

66 Rahimi E, Aramideh S, Han D, Gomez H, Ardekani AM. 2022. Transport and lymphatic uptake of monoclonal antibodies after subcutaneous injection. *Microvasc Res*. 139:104228.

67 Saadi W, *et al*. 2007. Generation of stable concentration gradients in 2D and 3D environments using a microfluidic ladder chamber. *Biomed Microdevices*. 9(5):627–635.

68 Tanner K. 2019. High frequency active microrheology reveals mismatch in 3D tumor intracellular and extracellular matrix viscoelasticity. *Biophys J*. 116(3):8a.

69 Brodin B, Steffansen B, Nielsen CU. 2010. Passive diffusion of drug substances: the concepts of flux and permeability. In: Brodin B, Steffansen B. Nielsen CU, editors. *Molecular biopharmaceutics*. London, UK: Pharmaceutical Press. p. 135–152.

70 Burdine N. 1953. Relative permeability calculations from pore size distribution data. *J Pet Technol*. 5(03):71–78.

71 Wang F, Imoto K. 1992. Pore size and negative charge as structural determinants of permeability in the torpedo nicotinic acetylcholine receptor channel. *Proc R Soc London Ser B, Biol Sci*. 250(1327):11–17.